Nano Research

Open Access

Research Article

A self-healing nanocatalytic hydrogel enables intraocular chemosensitization through oxidative stress amplification in uveal melanoma

Shuyan Qin[1,2,§], Lingyan Hua[2,§], Mengyao Li[3,4,§], Yuxiao Chen[3,4,§], Xianming Zhang[5], Shuhan Chen[5] ✉, Ai Zhuang[3,4] ✉, and Yanfeng Zeng[1] ✉

[1] *Lixiang Eye Hospital of Soochow University, Suzhou 215006, China*
[2] *Department of Ophthalmology, the Affiliated Suqian Hospital of Xuzhou Medical University, Suqian 223800, China*
[3] *Shanghai JiaoTong University School of Medicine, Shanghai 200025, China*
[4] *State Key Laboratory of Eye health, Department of Ophthalmology, Shanghai Ninth People's Hospital, Shanghai JiaoTong University School of Medicine, Shanghai 200011, China*
[5] *State Key Laboratory of High Performance Ceramics, Shanghai Institute of Ceramics, Chinese Academy of Sciences, Shanghai 200050, China*
[§] *Shuyan Qin, Lingyan Hua, Mengyao Li, and Yuxiao Chen contributed equally to this work.*

Cite this article: *Nano Research*, **2026**, *19*, 94908842. https://doi.org/10.26599/NR.2026.94908842

ABSTRACT: Uveal melanoma (UM), the most common primary intraocular malignancy in adults, faces significant therapeutic challenges due to chemoresistance and high metastatic potential. Although melphalan (Mel), a DNA-alkylating agent, is used for local tumor control, its efficacy is limited by drug resistance and retinal toxicity. Here, we report an injectable nanocatalytic hydrogel system (PS@LDO/Mel) designed to enhance chemosensitization by synergizing reactive oxygen species (ROS) generation and glutathione (GSH) depletion. The system integrates manganese-doped layered double oxide (MgFeMn-LDO) with Mel within a thiol-maleimide hydrogel, enabling controlled drug release and intraocular localization. Mn/Fe multimetallic synergy in MgFeMn-LDO enhanced GSH depletion by 15.15-fold compared to undoped MgFe-LDO within 60 min. *In vitro* studies demonstrated that PS@LDO/Mel elevated ROS levels and reduced GSH content, increasing apoptosis rates in OMM2.3 cells from 33.3% (Mel alone) to 70.1% while suppressing cell invasion. In murine models, the system effectively inhibited primary tumor growth through amplified DNA damage and mitochondrial apoptosis. By addressing limitations of conventional therapies, such as poor tumor targeting and uncontrolled drug release, this work provides a localized, multifunctional strategy for early-stage UM intervention, highlighting the potential of nanocatalytic hydrogels in ophthalmic oncology.

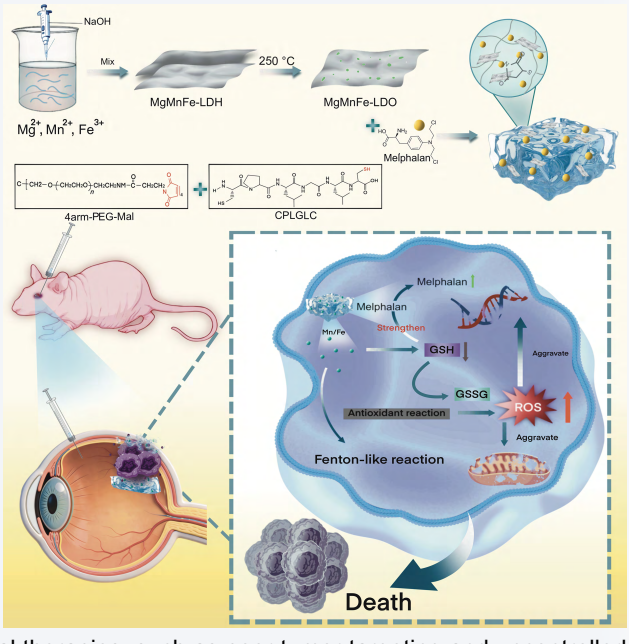

KEYWORDS: uveal melanoma, hydrogel, layered double hydroxide, chemosensitization, drug-controlled release

Received: December 31, 2025; **Revised:** May 13, 2026
Accepted: May 14, 2026

✉Address correspondence to Shuhan Chen, chenshuhan@mail.sic.ac.cn; Ai Zhuang, aizhuang@sjtu.edu.cn; Yanfeng Zeng, zengyanfeng@suda.edu.cn

1 Introduction

Uveal melanoma (UM), the most common primary intraocular malignancy in adults, is characterized by aggressive growth, pronounced chemoresistance, and a high propensity for fatal hepatic metastasis [1]. Chemotherapy, a cornerstone of comprehensive cancer treatment, shows limited efficacy in UM due

to its distinctive molecular landscape. Frequent *GNAQ*/*GNA11* mutations drive constitutive activation of the mitogen-activated protein kinase (MAPK) signaling pathway, while *BAP1* inactivation-associated epigenetic dysregulation and enhanced DNA repair capacity (e.g., homologous recombination) further attenuate chemosensitivity. Notably, the 5-year mortality rate exceeds 50% among UM patients with liver metastases, underscoring the urgent need for prophylactic chemotherapeutic intervention during the micrometastatic stage to suppress early tumor progression.

Melphalan (Mel), a nitrogen mustard alkylating agent, inhibits tumor proliferation by inducing DNA interstrand crosslinks. However, its clinical utility in UM is severely limited by intrinsic chemoresistance and retinal toxicity associated with intravitreal administration, restricting its application primarily to local tumor control or postoperative adjuvant therapy. Consequently, the development of advanced chemosensitization strategies capable of synergistically suppressing primary tumors while preventing metastatic dissemination remains a critical challenge in UM management.

Recent advances in nanocatalytic therapy have opened new avenues for precision oncology. This strategy employs enzyme-mimetic nanomaterials, such as metal-organic frameworks and transition-metal oxides, to trigger tumor-specific reactive oxygen species (ROS) generation and deplete endogenous antioxidants, particularly glutathione (GSH), thereby potentiating chemotherapeutic cytotoxicity [2]. However, UM cells possess robust oxidative stress defense mechanisms, including superoxide dismutase overexpression and upregulated GSH biosynthesis, which substantially compromise therapeutic efficacy [3]. Therefore, the rational design of nanocatalytic systems capable of simultaneous ROS amplification and GSH depletion is essential for effective UM chemosensitization.

Layered double hydroxides (LDHs) and their calcined derivatives (LDOs) have emerged as promising platforms for catalytic-chemotherapeutic synergy owing to their tunable composition, ion-exchange capacity, and redox activity [4]. Incorporation of transition metals (e.g., Mn, Fe) enables the construction of multivalent redox couples that enhance peroxidase-like catalytic activity and GSH oxidation efficiency [5]. Nevertheless, conventional LDH-based systems often suffer from poor tumor retention, uncontrolled drug release, and off-target toxicity, which limit their applicability for intraocular therapy.

Hydrogels, three-dimensional network materials with excellent biocompatibility, offer a viable solution to these challenges [6]. Integration of nanomaterials into hydrogel matrices improves intratumoral retention, enables high drug-loading capacity, and allows precise regulation of drug release kinetics through rational structural design [7]. An ideal ophthalmic hydrogel should satisfy several stringent criteria, including (i) injectability through 26-gauge needles (inner diameter ~ 0.26 mm), (ii) rapid sol-gel transition for *in situ* formation, and (iii) shear-thinning and self-healing properties to maintain structural integrity under physiological conditions.

In this study, we developed an injectable hydrogel based on thiol-maleimide Michael addition chemistry, co-loaded with manganese-doped LDO (MgFeMn-LDO) and melphalan to construct a multifunctional nanocatalytic platform (PS@LDO/Mel). Multimetallic Mn/Fe synergy enhanced the GSH depletion efficiency of MgFeMn-LDO by 15.15-fold compared with undoped MgFe-LDO within 60 min. *In vitro* experiments demonstrated that PS@LDO/Mel significantly elevated intracellular ROS levels while depleting GSH, increasing the early/late apoptosis rate of OMM2.3 cells from 33.3% (PS@Mel alone) to 70.1%, accompanied by marked suppression of cell invasion. Furthermore, *in situ* murine models validated its efficacy in inhibiting primary tumor growth, mediated by amplified DNA damage and mitochondria-dependent apoptotic pathways through chemocatalytic synergy. Collectively, this work presents a localized therapeutic strategy for early-stage UM intervention and advances the development of ophthalmic nanocatalytic medicine.

2 Experimental

2.1 Metal nanomases preparation and characterization

2.1.1 Preparation of LDO

The required masses and molar ratios of $MgCl_2{\cdot}6H_2O$, $MnCl_2{\cdot}4H_2O$, and $FeCl_3$ for four samples were calculated as shown in Table S1 in the Electronic Supplementary Material (ESM).

The mixtures were dissolved in 200 mL of ultrapure water, followed by addition of 3.2 mL 10 M NaOH solution under continuous stirring for 30 min to obtain LDH suspensions. The resultant suspensions were centrifuged at 4500 rpm for 5 min and sequentially washed twice with ultrapure water and once with anhydrous ethanol. The collected precipitates were dried at 60 °C for 12 h in an oven, yielding MgFe-LDH, $MgMn_1$Fe-LDH, $MgMn_2$Fe-LDH, and $MgMn_3$Fe-LDH powders.

The dried powders were ground into fine particles and calcined in a muffle furnace under static air. The temperature was raised to 250 °C at a heating rate of 5 °C/min and maintained for 5 h. The final products (MgFe-LDO, $MgMn_1$Fe-LDO, $MgMn_2$Fe-LDO, and $MgMn_3$Fe-LDO) were collected after cooling to below 100 °C.

2.1.2 TEM characterization of LDO

Aqueous dispersions of MgFe-LDO and $MgMn_3$Fe-LDO (200 μg/mL) were drop-casted onto copper grids and air-dried. The morphology of the samples was observed using transmission electron microscopy (TEM, Tecnai G2 F20, USA) operated at 120 kV and 70 μA. High-angle annular dark-field (HAADF) imaging and elemental mapping were further analyzed to investigate the microstructure and elemental distribution. For structural analysis, uncalcined MgFe-LDH and $MgMn_3$Fe-LDH powders, as well as calcined MgFe-LDO and $MgMn_3$Fe-LDO powders, were uniformly spread on the sample holder of an X-ray diffractometer (XRD, D2 Advance, Bruker, Germany). XRD patterns were collected over a 2θ range of 5°–80° (Fig. 1(b)) and 10°–80° (Fig. 1(c)) with a step size of 0.02°.

2.1.3 Evaluation of catalytic performance of enzymes

2.1.3.1 Peroxidase-like Activity Assay

A 1 mg/mL LDO ultrapure aqueous dispersion was prepared and sonicated for 4 h until the LDO powder was mostly dispersed. Subsequently, 200 μL of the LDO dispersion was mixed with 200 μL of hydrogen peroxide (H_2O_2) and 200 μL of 3,3',5,5'-tetramethylbenzidine (TMB, 20 mM) chromogenic solution. The mixtures were then added to 1400 μL of sodium acetate-acetic acid (NaAc-HAc) buffer (pH = 6.0) and 1400 μL of NaAc-HAc buffer (pH = 7.4), respectively. After thorough vortexing, the solutions

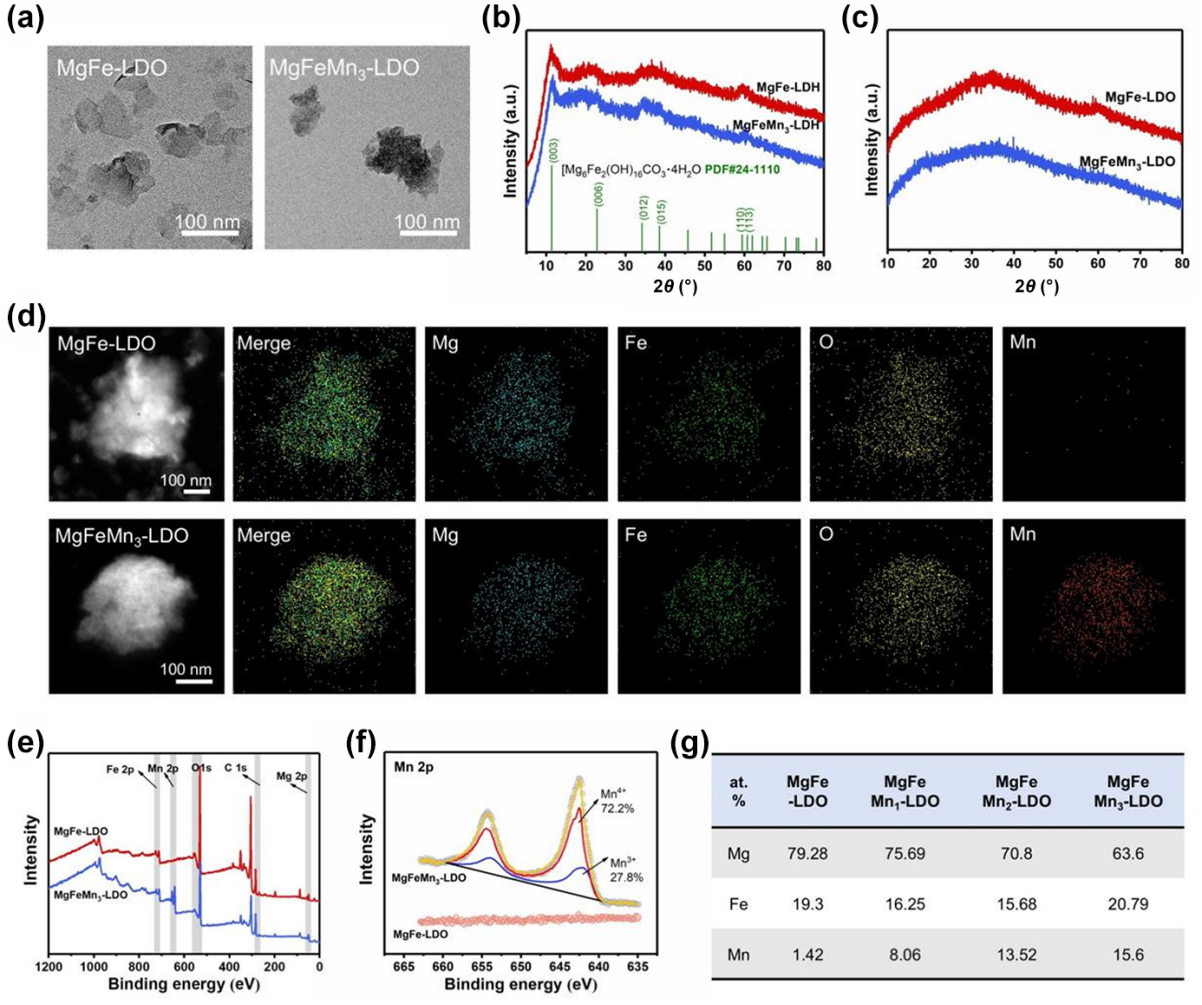

(g)

at. %	MgFe -LDO	MgFe Mn_1-LDO	MgFe Mn_2-LDO	MgFe Mn_3-LDO
Mg	79.28	75.69	70.8	63.6
Fe	19.3	16.25	15.68	20.79
Mn	1.42	8.06	13.52	15.6

Figure 1 Synthesis and characterization of Mn-doped layered double oxides. (a) TEM images of MgFe-LDO and $MgFeMn_3$-LDO. (b) XRD patterns of MgFe-LDH and $MgFeMn_3$-LDH. (c) XRD patterns of MgFe-LDO and $MgFeMn_3$-LDO. (d) TEM elemental mapping of MgFe-LDO and $MgFeMn_3$-LDO. (e) Spectral analysis of XPS. (f) High resolution spectra of Mn 2p. (g) Atomic percentages (at.%) of Mg, Fe, and Mn in LDOs.

were incubated in the dark at 37 °C for 10, 20, 30, and 60 min. Finally, 100 μL of each reaction solution was transferred to a 96-well plate, and the absorption spectra (500–800 nm) as well as the absorbance at 652 nm were measured using a microplate reader.

2.1.3.2 Oxidase-like activity assay

200 μL of each of the four LDO dispersions (1 mg/mL) was mixed with 200 μL of TMB chromogenic solution (20 mM). The mixtures were then added to 1600 μL of NaAc-HAc buffer (pH = 6.0) or 1600 μL of NaAc-HAc buffer (pH = 7.4), respectively. After thorough vortexing, the solutions were incubated in the dark at 37 °C for 10, 20, 30, and 60 min. The absorption spectra (500–800 nm) were measured using a microplate reader.

2.1.4 GSH depletion capacity evaluation

2.1.4.1 GSH standard curve determination

A 1 mg/mL 5,5'-dithiobis-(2-nitrobenzoic acid) (DTNB) chromogenic solution was prepared and stored in the dark. A 40 mM GSH solution was prepared by dissolving 122.9 mg of GSH powder in 10 mL of ultrapure water, followed by serial dilution to obtain 2, 1, 0.5, 0.25, 0.125, and 0 mM GSH solutions. For the assay, 50 μL of DTNB solution was mixed with 50 μL of each GSH solution in a 96-well plate. After 5 min of reaction at room temperature, the absorbance at 452 nm was measured using a microplate reader. A standard curve was generated using the obtained data.

2.1.4.2 GSH depletion capacity of MgFe-LDO and MgFeMn-LDO

A 2 mM GSH solution was used for the following experiments. Solution A was prepared by mixing 100 μL of 2 mM GSH solution, 200 μL of LDO dispersion, and 700 μL of NaAc-HAc buffer (pH = 6.0). Then, 50 μL of Solution A was combined with 50 μL of DTNB solution in a 96-well plate. After 5 min of reaction at room temperature, the absorbance at 452 nm was recorded as A. For the background control (A_b), 50 μL of Solution A was mixed with 50 μL of NaAc-HAc buffer (pH = 6.0), incubated for 5 min, and measured at 452 nm. Absorption spectra (500–800 nm) were also recorded. GSH depletion capacity was calculated using the equation (Eq. (1)):

$$\text{GSH depletion}\ (\%) = \left(\frac{A - A_b}{A_0 - A_b}\right) \times 100 \quad (1)$$

where A, A_0 (negative control), and A_b (positive control) represent the absorbance values at 452 nm.

2.1.5 ROS generation evaluation

2.1.5.1 Total ROS detection using 2',7'-dichlorodihydrofluorescein diacetate (DCFH-DA)

A 0.01 M NaOH solution was prepared by dissolving 8 mg of NaOH in 20 mL of ultrapure water. A 50 μL aliquot of 20 mM DCFH-DA (Sigma-Aldrich, Germany) was mixed with 200 μL of 0.01 M NaOH and incubated in the dark for 30 min. The reaction was terminated by adding 1 mL of NaAc-HAc buffer (pH = 7.4) to obtain DCFH solution. The target solution was obtained by mixing DCFH solution, LDO water dispersion solution (1 mg/mL) and NaAc-HAc buffer solution with pH = 6.0 in different proportions (Table S2 in the ESM). At 30, 60, 120, and 360 min, 100 μL of each solution was transferred to a 96-well plate. Fluorescence intensity was measured at 530 nm (excitation: 488 nm), and emission spectra (508–650 nm, 5 nm steps) were recorded.

2.1.5.2 Superoxide anion ($\cdot O_2^-$) detection using dihydroethidium (DHE)

Three target solutions were obtained by mixing DHE (0.1 mg/mL) solution in different proportions, NaAc-HAc buffer with pH = 6.0, and LDO (1 mg/mL) dispersed aqueous solution (Table S3 in the ESM). At 5, 15, 30, and 60 min, 100 μL of each solution was added to a 96-well plate. Fluorescence intensity was measured at 425 nm (excitation: 350 nm), and emission spectra (370–600 nm, 5 nm steps) were recorded.

2.2 Hydrogel preparation and characterization

2.2.1 Hydrogel synthesis

Solutions were prepared as follows: 100 mg/mL four-arm PEG-maleimide (4arm-PEG-Mal, M_W = 10,000, ≥ 95% purity, Adamas Life); 20 mg/mL CPLGLC polypeptide (SH-R, ≥ 95% purity, Hefei Guopei Biotech); 10 mg/mL $MgMn_3Fe$-LDO (abbreviated as LDO); 20 mM Mel. For 1 mL hydrogel samples, the components were mixed according to Table S4 in the ESM. After homogenization, the mixtures were allowed to stand for 24 h to form hydrogels.

2.2.2 Injectable hydrogel property evaluation

2.2.2.1 Rheological analysis

Hydrogels (5–8 mm diameter, 1.2–2 mm thickness) were analyzed using an MCR301 rheometer (Anton Parr, Austria). Storage modulus (G') and loss modulus (G'') were measured under frequency sweeps (0.1–100 Hz, 1% strain) and strain sweeps (0.1%–1000%, 1 Hz) at 25 °C.

2.2.2.2 Self-healing capacity

PS@LDO/Mel hydrogels were stained with methylene blue trihydrate (1 mg/mL), phenol red (1 mg/mL), or Orange II (1 mg/mL). Stained hydrogels were injected into culture dishes or reassembled after cutting. Self-healing was visually confirmed and photographed.

2.2.3 Surface functional group characterization

Freeze-dried hydrogels were analyzed using a Fourier transform infrared spectrometer (FTIR, Tensor 27, Bruker, Germany).

2.2.4 Scanning electron microscopy (SEM) imaging

The freeze-dried samples were first quenched in liquid nitrogen for 1 min to achieve brittle fracture. Subsequently, the samples were manually fractured to expose relatively smooth cross-sectional surfaces. These freshly exposed surfaces were then mounted on conductive carbon tape and sputter-coated with a thin platinum layer using a vacuum coating system (MSP-1S, Shinkuu Device, Japan) to enhance surface conductivity. Cross-sectional morphology characterization was performed using a tungsten-filament SEM (S-3400N, Hitachi, Japan) operating at an accelerating voltage of 15 kV.

2.2.5 Hydrogel GSH depletion capacity

A 2 mM GSH solution was prepared by mixing 200 μL of 20 mM GSH stock solution (Sigma-Aldrich, USA) with 1.8 mL sodium acetate-acetic acid (NaAc-HAc) buffer (pH 6.0, 0.1 M). Hydrogel specimens (100 μL) were fully immersed in the prepared GSH solution and maintained at 37 °C under static conditions. Supernatant aliquots (50 μL) were collected at predetermined degradation intervals (12, 24, and 48 h), then mixed with 50 μL 5,5'-dithiobis-(2-nitrobenzoic acid) (DTNB, 2 mg/mL in ethanol, Aladdin, China) to initiate chromogenic reaction. After 5 min incubation at ambient temperature, the mixture was transferred to a 96-well plate (Corning, USA) for absorbance measurement at 452 nm using a microplate reader (Multiskan GO, Thermo Scientific, USA).

2.3 Cell culture

2.3.1 PS@LDO/Mel hydrogel drug release analysis

Hydrogels (100 μL) were placed in Transwell inserts (LABSELECT, PC membrane) over 2 mL phosphate-buffered saline (PBS). Released drug in PBS was quantified via ultraviolet–visible (UV–Vis) spectroscopy at days 0–5.

2.3.2 Cell model establishment

The cytocompatibility and pro-apoptotic efficacy of drug-loaded hydrogels were assessed using human retinal pigment epithelial cells (ARPE-19, CRL-2302, American Type Culture Collection (ATCC)) and uveal melanoma cells (OMM2.3, CVCL_6944, Leibniz Institute DSMZ-German Collection of Microorganisms and Cell Cultures (DSMZ)). ARPE-19 cells were maintained in Dulbecco's modified Eagle medium (DMEM) complete medium (Gibco, USA) supplemented with 10% fetal bovine serum (FBS, Gibco, USA) and 1% Penicillin-Streptomycin (HyClone, USA), while OMM2.3 cells were cultured in Roswell Park Memorial Institute 1640 medium (RPMI-1640) (Corning, USA) containing identical serum and antibiotic concentrations. All cell cultures were incubated under standardized conditions (5% CO_2, 95% humidity, 37 °C) in a water-jacketed incubator (Heracell 150i, Thermo Scientific, USA).

Cell culture maintenance included twice-daily medium replacement and subculturing at 80% confluence using 0.25% trypsin-EDTA (Solarbio, China). Cells between passages 3–5 were employed for experimental procedures to ensure phenotypic stability. Hydrogel specimens (Φ 6 mm × 2 mm) were sterilized by UV irradiation (30 min per side) prior to cell contact.

2.3.3 Cellular drug concentration determination

ARPE-19 and OMM2.3 cells were treated with PS@Mel hydrogels (0.5–2 mM Mel). Cell viability was assessed via AlamarBlue™ and live/dead staining.

2.3.4 Cell invasion assay

Following trypsinization with 0.25% trypsin-EDTA (Solarbio, China), OMM2.3 cells were collected via centrifugation (1000 rpm, 5 min) and resuspended in serum-free RPMI-1640 medium (Corning, USA). Cell suspensions (200 μL containing 5 × 10^5 cells/mL) were seeded into the upper chambers of 8 μm pore Transwell® inserts (Corning, USA). Four hydrogel formulations (PS, PS@LDO, PS@Mel, and PS@LDO/Mel) were prepared by mixing 100 μL hydrogel with 800 μL complete medium (RPMI-1640 containing 10% FBS and 1% Penicillin-Streptomycin), which was then added to the lower chamber. After incubation under standard culture conditions (5% CO_2, 95% humidity, 37 °C) for 12–48 h, cell invasion dynamics were monitored using phase-contrast microscopy (DMi8, Leica, Germany). At designated timepoints, non-invading cells on the upper membrane surface were removed using sterile cotton swabs. Invaded cells were fixed with 4% paraformaldehyde (Beyotime, China) for 15 min, washed twice with PBS (HyClone, USA), and stained with 1% crystal violet (Sigma-Aldrich, USA) for 30 min at ambient temperature. Following final PBS rinses, membranes were air-dried and imaged under an inverted microscope (CKX53, Olympus, Japan). Invasion quantification was performed using ImageJ 1.53t (NIH, USA) by calculating the ratio of crystal violet-positive area to total membrane area.

2.3.5 Intracellular GSH content

Cell lysates were mixed with GSH assay reagents (A006-2-1, Nanjing Jiancheng Bioengineering Institute). Absorbance at 405 nm was measured, and GSH levels were normalized to protein concentration.

2.3.6 Mitochondrial membrane potential (JC-1 assay)

Following trypsinization with 0.25% trypsin-EDTA (Solarbio, China), OMM2.3 cells were collected via centrifugation (1000 rpm, 5 min) and resuspended in serum-free RPMI-1640 medium (Corning, USA). Cell suspensions (200 μL containing 5 × 10^5 cells/mL) were seeded into the upper chambers of 8 μm pore Transwell® inserts (Corning, USA). Four hydrogel formulations (PS, PS@LDO, PS@Mel, and PS@LDO/Mel) were prepared by mixing 100 μL hydrogel with 800 μL complete medium (RPMI-1640 containing 10% FBS and 1% Penicillin-Streptomycin), which was then added to the lower chamber. After incubation under standard culture conditions (5% CO_2, 95% humidity, 37 °C) for 12–48 h, cell invasion dynamics were monitored using phase-contrast microscopy (DMi8, Leica, Germany). At designated timepoints, non-invading cells on the upper membrane surface were removed using sterile cotton swabs. Invaded cells were fixed with 4% paraformaldehyde (Beyotime, China) for 15 min, washed twice with PBS (HyClone, USA), and stained with 1% crystal violet (Sigma-Aldrich, USA) for 30 min at ambient temperature. Following final PBS rinses, membranes were air-dried and imaged under an inverted microscope (CKX53, Olympus, Japan). Invasion quantification was performed using ImageJ 1.53t (NIH, USA) by calculating the ratio of crystal violet-positive area to total membrane area.

2.3.7 Intracellular ROS detection

UM cells were inoculated into 24-well plates at a density of 50,000 cells/mL and then cultured in a cell constant temperature incubator for 24 h before changing the medium. The pre-prepared hydrogel was placed in the Transwell chamber and co-cultured with the cells. Then the cells were gently washed twice with PBS. Then, 500 μL of DCFH-DA (10 μM, Sigma-Aldrich, Germany) solution was added to stain the intracellular ROS. The cells were incubated in the dark at 37 °C for 30 min and washed three times with PBS. The green fluorescence field was observed under a fluorescence microscope.

2.3.8 Flow cytometry

OMM2.3 cells were trypsinized, resuspended in PBS, and analyzed using a flow cytometer. After resuspension and counting, cells were adjusted to the target concentration. The cell suspension was incubated with 5 μL Annexin V-fluorescein isothiocyanate (FITC) and 5 μL propidium iodide (PI) for 10 min in the dark. Prior to flow cytometry analysis, system verification was performed using a BD FACSCanto™ flow cytometer: Firstly, confirmed proper sheath fluid (FACSFlow™) and waste tank levels. Secondly, executed CS&T quality control to calibrate the 633 nm laser. Finally, selected 488 nm (blue) and 633 nm (red) detection channels, adjusting voltage to position the negative population within the 10–100. Gated using FSC/SSC scatter plots to exclude debris and cell aggregates. Cell subpopulations were classified as follows: Q1 (lower-left quadrant), Q2 (lower-right quadrant), and Q3 (upper-right quadrant). The data was acquired using FACSDiva™ software and analyzed with FlowJo® v10.8.

2.4 Animal behavioral experiments

UM cells (2 × 10^5 cells) were injected into the subretinal space of mice to establish ocular tumors. Ten days post-inoculation, the mice were administered 3 μL of sterile PBS, PS, PS@LDO, PS@Mel and PS@LDO/Mel. On day 20 post-treatment, the eyeballs, heart, liver, kidneys, lungs, and spleen were harvested for histological sectioning and hematoxylin and eosin (H&E) staining.

2.5 Data analysis

Statistical significance (P) was determined through one-way ANOVA with Tukey's post-hoc test using GraphPad Prism 9 software. $P < 0.05$ was considered statistically significant and was denoted by $^*P < 0.05$, $^{**}P < 0.01$, $^{***}P < 0.001$, and $^{****}P < 0.0001$.

3 Results and discussion

3.1 Preparation and characterization of Mn-doped ternary layered metal oxides

LDHs and their derivatives are two-dimensional nanomaterials characterized by high specific surface area, strong ion-exchange capacity, and a layered structure. The interlayer space can accommodate chemotherapeutic agents or nanoparticles, enhancing chemodynamic therapeutic efficacy in clinical applications [8]. Previous studies indicate that nanomaterials, owing to their larger surface area, accelerate chemodynamic reactions more effectively than micron-sized materials [9]. As shown in Fig. 1(a), LDHs were synthesized via a coprecipitation method and subsequently calcined at 250 °C to obtain LDOs [10]. Based on Mn doping levels, the samples were labeled as MgFe-LDO, $MgFeMn_1$-LDO, $MgFeMn_2$-LDO, and $MgFeMn_3$-LDO. Mn doping replaces partial Mg ions, forming ternary MgFeMn-LDO.

The XRD patterns (Fig. 1(b)) of MgFe-LDH and $MgFeMn_3$-LDH exhibit characteristic (003), (006), and (009) diffraction peaks

at 11.1°, 20.7°, and 34.0°, respectively, confirming successful LDH synthesis. After calcination (Fig. 1(c)), these peaks disappeared, and amorphous structural features emerged, indicating LDH-to-LDO transformation. TEM images (Fig. 1(d)) revealed lamellar structures for both MgFe-LDO and $MgFeMn_3$-LDO, with uniform distribution of Mg, Fe, and O. Mn was homogeneously incorporated in $MgFeMn_3$-LDO, confirming successful doping.

X-ray photoelectron spectroscopy (XPS) survey spectra (Fig. 1(e)) of MgFe-LDO and $MgFeMn_3$-LDO showed characteristic peaks for Mg 2p (48.5 eV), Fe 2p (710.9 eV), O 1s (529.8 eV), and C 1s (284.8 eV). The C 1s peak originated from surface carbon contamination. $MgFeMn_3$-LDO exhibited an additional Mn 2p peak at 642.3 eV, verifying Mn incorporation. High-resolution Mn 2p spectra (Fig. 1(f)) further confirmed Mn doping. Peak deconvolution revealed the coexistence of Mn^{3+} and Mn^{4+} species, indicating the formation of multivalent redox centers within the oxide lattice. The high-resolution spectra of Fe 2p, Mg 2p, and O 1s (Fig. S1 in the ESM) further clarified the chemical states of the constituent elements. Fe was predominantly present as Fe^{3+}, while Mg 2p at 49.7 eV was assigned to Mg^{2+} in an oxide environment. The O 1s spectrum consisted of lattice M–O and surface M–OH components, suggesting partial dehydroxylation during calcination while retaining abundant hydroxyl groups. The coexistence of multivalent Mn species, Fe^{3+} centers, lattice oxygen, and surface hydroxyl groups collectively provides favorable conditions for electron transfer and reactive oxygen species generation. Quantitative analysis (Fig. 1(g)) revealed that Mn atomic percentages increased from 1.42 at.% to 15.6 at.%, while Mg decreased from 79.28 at.% to 63.6 at.%, correlating with Mn precursor concentration.

3.2 Enzyme-mimetic catalytic activity of Mn-doped layered metal oxides

Layered metal oxides exhibit redox activities analogous to oxidase (OXD), peroxidase (POD), and superoxide dismutase (SOD), and are therefore classified as "nanozymes" due to their tunable metal compositions. Compared with natural enzymes, these nanozymes offer distinct advantages, including cost-effectiveness, high stability, and adjustable catalytic activity. Furthermore, strategies such as morphology regulation, surface modification, and heteroatom doping have been widely employed to further enhance their enzyme-like performance [11].

TMB chromogenic assays demonstrated the pH-dependent OXD-like activity of LDOs [12]. Under tumor-mimicking acidic conditions (pH = 6.0), Mn-doped LDOs exhibited markedly enhanced OXD-like (Figs. 2(a) and 2(b), and Figs. S2 and S3 in the ESM) and POD-like (Figs. 2(c) and 2(d), and Figs. S4 and S5 in the ESM) activities compared with those observed under physiological conditions (pH = 7.4), thereby minimizing potential off-target toxicity. In contrast, MgFe-LDO displayed relatively weak ROS generation and GSH consumption capabilities.

Mn doping significantly elevated the redox activity of LDOs. Notably, the GSH consumption capacity of $MgFeMn_3$-LDO was 15.15-, 3.37-, and 3.24-fold higher than that of MgFe-LDO at 60, 120, and 360 min, respectively. These results indicate that Mn incorporation enhances both the kinetics and total capacity of GSH depletion. The amplified catalytic activity observed with increasing Mn content can be attributed to the formation of multivalent $Mn^{2+}/Mn^{3+}/Mn^{4+}$ and Fe^{2+}/Fe^{3+} redox couples. Moreover, the enzyme-like catalytic activity of LDOs increased progressively with prolonged reaction time.

To identify the specific ROS generated, DHE and DCFH-DA probes were employed to detect ROS species and overall levels, respectively. Under weakly acidic conditions, MgFeMn-LDO actively consumed O_2 and generated cytotoxic superoxide radicals ($\cdot O_2^-$) (Figs. 2(e) and 2(f)), accompanied by a significant elevation in total ROS levels (Figs. 2(g) and 2(h)). This enhanced ROS production is expected to substantially improve tumor cell-killing efficacy.

GSH, a critical intracellular antioxidant and free-radical scavenger, plays a pivotal role in protecting tumor cells from ROS-induced oxidative damage [13]. Therefore, depletion of GSH can effectively amplify ROS-mediated tumor cell destruction. Owing to the presence of multivalent metal ion pairs, the GSH-depleting capability of MgFeMn-LDO was markedly enhanced (Figs. 2(i) and 2(j)), further disrupting redox homeostasis within tumor cells.

In addition, Mn doping significantly improved the O_2 generation capacity of the material in the presence of hydrogen peroxide (Fig. 2(k)), which is beneficial for alleviating tumor hypoxia [14]. Collectively, the outstanding ROS generation, GSH depletion, and O_2 production capabilities of MgFeMn-LDO are expected to collapse the intracellular antioxidant defense system and accelerate tumor cell apoptosis.

3.3 Synthesis of chemosensitizing nanocatalytic hydrogels

For ocular applications, hydrogels must be injectable via a 1 mL Hamilton microinjector into the subchoroidal space and rapidly recover their gel state post-injection to maintain functionality [14]. Thus, the synthesized hydrogels require robust gelation kinetics, injectability, and self-healing properties.

In this study, maleimide-terminated 4arm-PEG-Mal was used at a final concentration of 3.5% (w/v), with crosslinker addition controlled by the maleimide-to-thiol (Mal/SH) molar ratio (final concentration: 0.28%). As illustrated in Fig. 3(a), the hydrogel (denoted PS@LDO/Mel) was synthesized via Michael addition between thiol groups in the crosslinker and maleimide groups in 4arm-PEG-Mal, co-loaded with LDO and Mel. FTIR spectra (Fig. 3(b)) confirmed characteristic functional groups (–C–H–, –C=O/–N–H–, and –C–O–) in all hydrogels. All formulations retained structural integrity without flow after 24 h of inversion (Fig. 3(c)), confirming successful gelation. The incorporation of LDO and Mel did not disrupt the hydrogel matrix.

PS@LDO/Mel exhibited excellent injectability and self-healing (Fig. 3(d)), attributed to abundant hydrogen bonding, enabling smooth extrusion through a 1 mL Hamilton microinjector needle [15]. SEM images of hydrogel cross-sections (Fig. 3(e)) revealed a porous structure in PS and PS@LDO hydrogels. In contrast, the apparent porosity was markedly reduced after Mel incorporation, which is more reasonably attributed to increased network density and polymer packing induced by Mel-polymer interactions.

Rheological analysis quantified the storage modulus (G', energy storage during elastic deformation) and loss modulus (G'' energy dissipation during viscous flow). The ratio of G' to G'' determines gel state transitions: $G' > G''$ indicates a gel state, while $G'' > G'$ suggests sol formation. As shown in Figs. 3(f) and 3(g), all hydrogels maintained $G' > G''$ under high strain (1000%) and frequency (10 Hz), demonstrating mechanical resilience suitable for intraocular applications under physiological pressure.

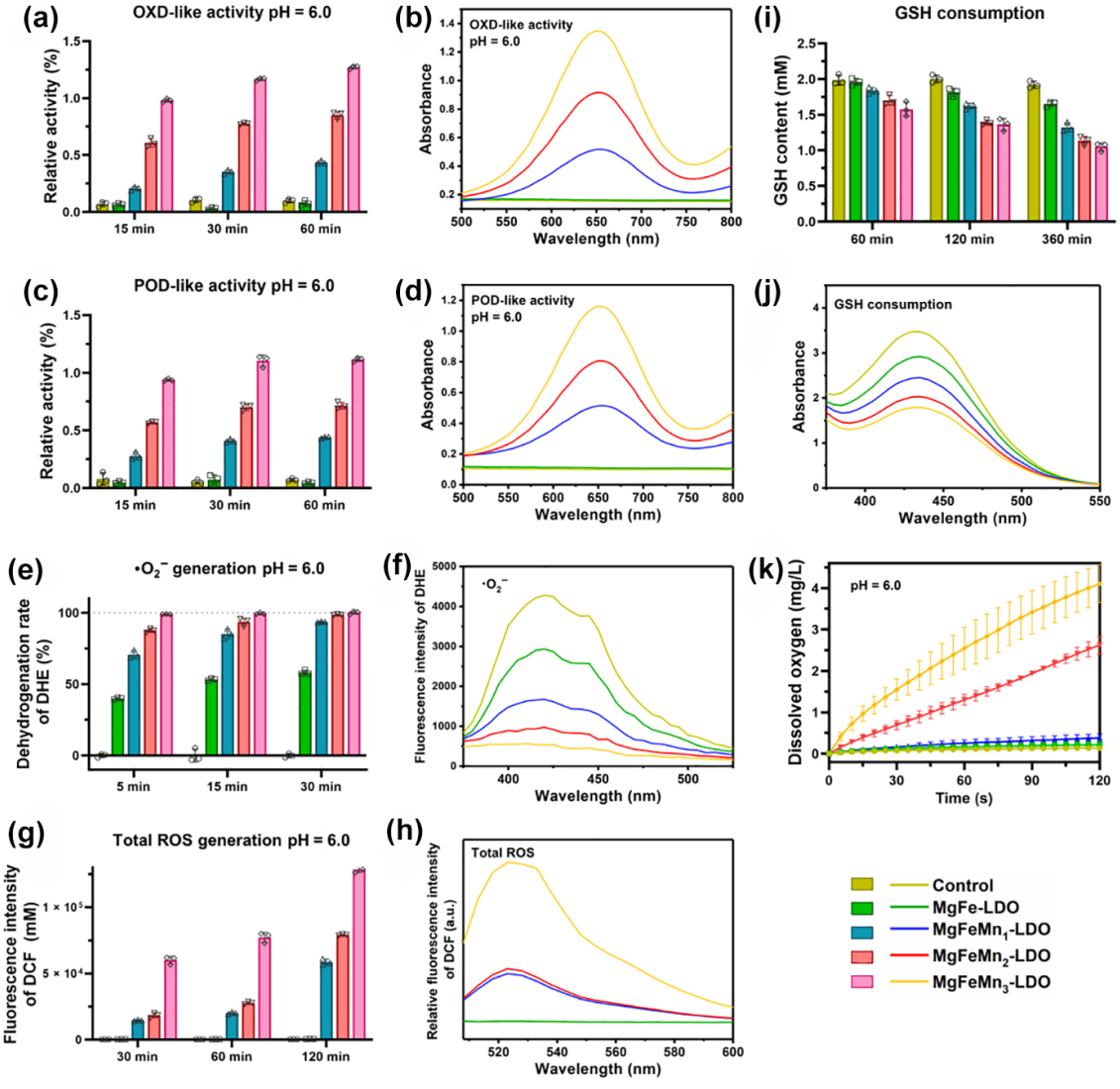

Figure 2 Catalytic ROS generation and GSH depletion of Mn-doped LDOs. OXD-like activity of Mn-doped LDO: (a) absorbance at 652 nm and (b) absorption spectra. POD-like activity of Mn-doped LDO: (c) absorbance at 652 nm and (d) absorption spectra. (e) Superoxide anion ($\cdot O_2^-$) generation by Mn-doped LDO at pH = 6.0: fluorescence intensity (ex/em = 350/425 nm) and (f) emission spectra of DHE. Total ROS production by Mn-doped LDO at pH = 6.0: (g) fluorescence intensity (ex/em = 488/530 nm) and (h) emission spectra of DCF. GSH depletion capacity of Mn-doped LDO at pH = 6.0: (i) absorbance values and (j) DTNB absorption spectra. (k) Oxygen generation by Mn-doped LDO at pH = 6.0.

3.4 Antitumor efficacy of chemosensitizing nanocatalytic hydrogels

The rapid proliferation of tumor cells leads to elevated levels of ROS in the tumor microenvironment. To counteract this oxidative stress, tumor cells upregulate antioxidant systems, including superoxide dismutase, catalase, and GSH [16]. Catalytic chemotherapy sensitization leverages nanomaterials that trigger enzyme-like reactions in the tumor microenvironment to enhance therapeutic efficacy. In this study, we systematically evaluated the antitumor activity of a nanozyme-based catalytic hydrogel on OMM2.3 cells using various assays, including live/dead staining, cell viability measurements, and apoptosis detection. We specifically investigated intracellular GSH depletion, mitochondrial membrane potential (ΔΨm) using JC-1 staining, cell invasion capacity, and ROS production to comprehensively assess the hydrogel's antitumor effects.

In the PS@LDO/Mel hydrogel, manganese doping enhanced the catalytic generation of ROS, which synergized with the chemotherapeutic agent melphalan to improve antitumor efficacy [17]. Additionally, the hydrogel modulated drug release kinetics, increasing melphalan bioavailability and therapeutic performance [18]. As shown in Fig. 4(a), PS@Mel hydrogel released up to 700 μM of melphalan within the first day, gradually reaching 800 μM by day 5. In contrast, PS@LDO@Mel hydrogel exhibited reduced drug release (500 μM) on both days 1 and 5, likely due to strong hydrogen bonding between LDO and melphalan that delayed drug release.

GSH is a key intracellular antioxidant, and its depletion can impair the cell's ability to detoxify ROS, rendering tumor cells more susceptible to oxidative damage [19]. Since cancer cells often overexpress GSH to resist chemotherapy, we examined the hydrogel's GSH depletion capacity. PS@LDO hydrogel efficiently consumed GSH under acidic conditions in a time-dependent manner (Fig. 4(b)). Notably, PS@LDO/Mel hydrogel showed slightly reduced GSH depletion, possibly due to melphalan-induced

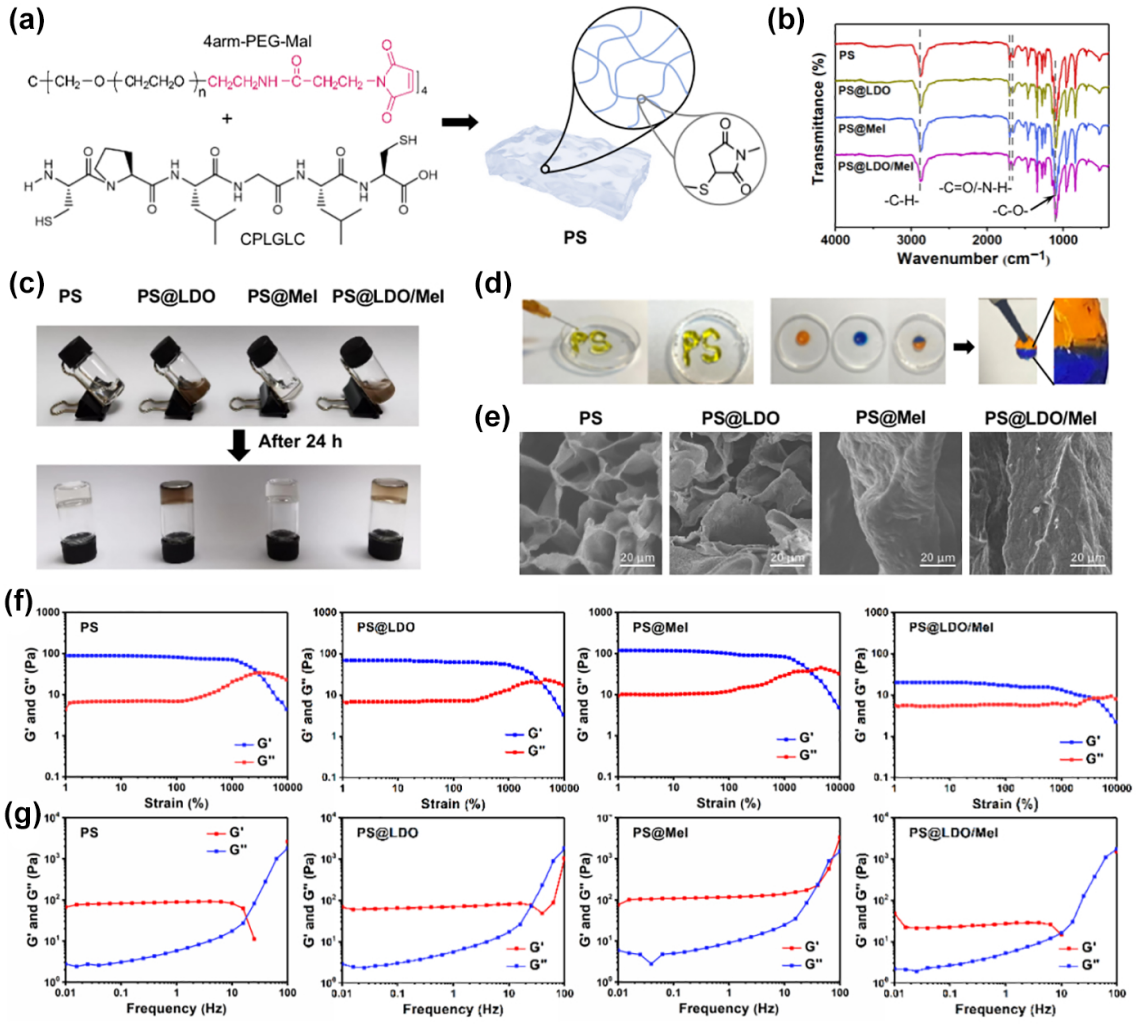

Figure 3 Injectable and self-healing nanocatalytic hydrogel. (a) Schematic illustration of PS hydrogel preparation. (b) FTIR spectra of hydrogels. (c) Optical images of hydrogels pre- and post-gelation. (d) Injectable and self-healing properties of PS hydrogel. (e) SEM images of hydrogel cross-sections. (f) Strain-dependent moduli (storage modulus *G'* and loss modulus *G''*) of hydrogels. (g) Frequency-dependent moduli of hydrogels.

alterations in hydrogel porosity, which limited GSH access to LDO. Nevertheless, PS@LDO/Mel achieved near-complete GSH depletion within 48 h. Intracellular GSH levels in OMM2.3 cells co-cultured with the hydrogels mirrored the non-cellular results (Fig. 4(c)).

We hypothesize that the enhanced antitumor effect of melphalan is mediated by LDO-induced ROS production and GSH consumption in UM cells. To assess tumor selectivity, we evaluated the cytotoxicity of the PS@LDO/Mel hydrogel (loaded with 1 mg/mL LDO and 2 mM melphalan) in both OMM2.3 cells and ARPE-19 retinal pigment epithelial cells. As shown in Figs. 4(d) and 4(e), and Figs. S6 and S7 in the ESM, the hydrogel significantly reduced OMM2.3 viability while sparing ARPE-19 cells. Flow cytometry further revealed that the rates of early/late apoptosis were 1.32%/3.27% (PS), 1.78%/10.5% (PS@LDO), 12%/21.3% (PS@Mel), and 37.8%/32.3% (PS@LDO/Mel) (Fig. 4(f)). These results suggest that Mn-doped PS@LDO and PS@melphalan cooperatively promote apoptosis and necrosis, likely due to increased ROS generation via nanozyme catalysis.

ROS accumulation can cause mitochondrial membrane depolarization, as indicated by the shift from red-fluorescent JC-1 aggregates (high ΔΨm) to green-fluorescent JC-1 monomers (low ΔΨm). As shown in Figs. 4(g) and 4(h), and Fig. S8 in the ESM, both PS@LDO and PS@LDO/Mel groups exhibited increased green and decreased red fluorescence, indicating reduced ΔΨm and early-stage apoptosis. ROS generation was further evaluated using the DCFH-DA probe. As shown in Figs. 4(i) and 4(j), the PS@LDO group produced mild fluorescence, while melphalan and PS@LDO@Mel groups showed strong green fluorescence, confirming elevated intracellular ROS levels. The spotted fluorescent pattern in the LDO@Mel group likely reflects ROS release from late apoptotic cells, consistent with apoptosis data.

Beyond apoptosis, the hydrogel may also suppress tumor cell invasiveness. As shown in Figs. 4(k) and 4(l), PS@LDO treatment reduced cell invasion area from 54.27% to 44.6%, and PS@LDO/Mel further decreased it from 2.24% to 0.06%. These findings indicate that LDO-loaded PS@Mel hydrogels significantly impair UM cell invasion, potentially through GSH depletion and ROS enhancement.

3.5 PS@LDO/Mel enhances chemotherapy in UM mouse models

A UM periocular tumor model was established by injecting OMM2.3/Luc cells into the orbital region of mice. Starting on day 10 post-model establishment, mice were randomized into five

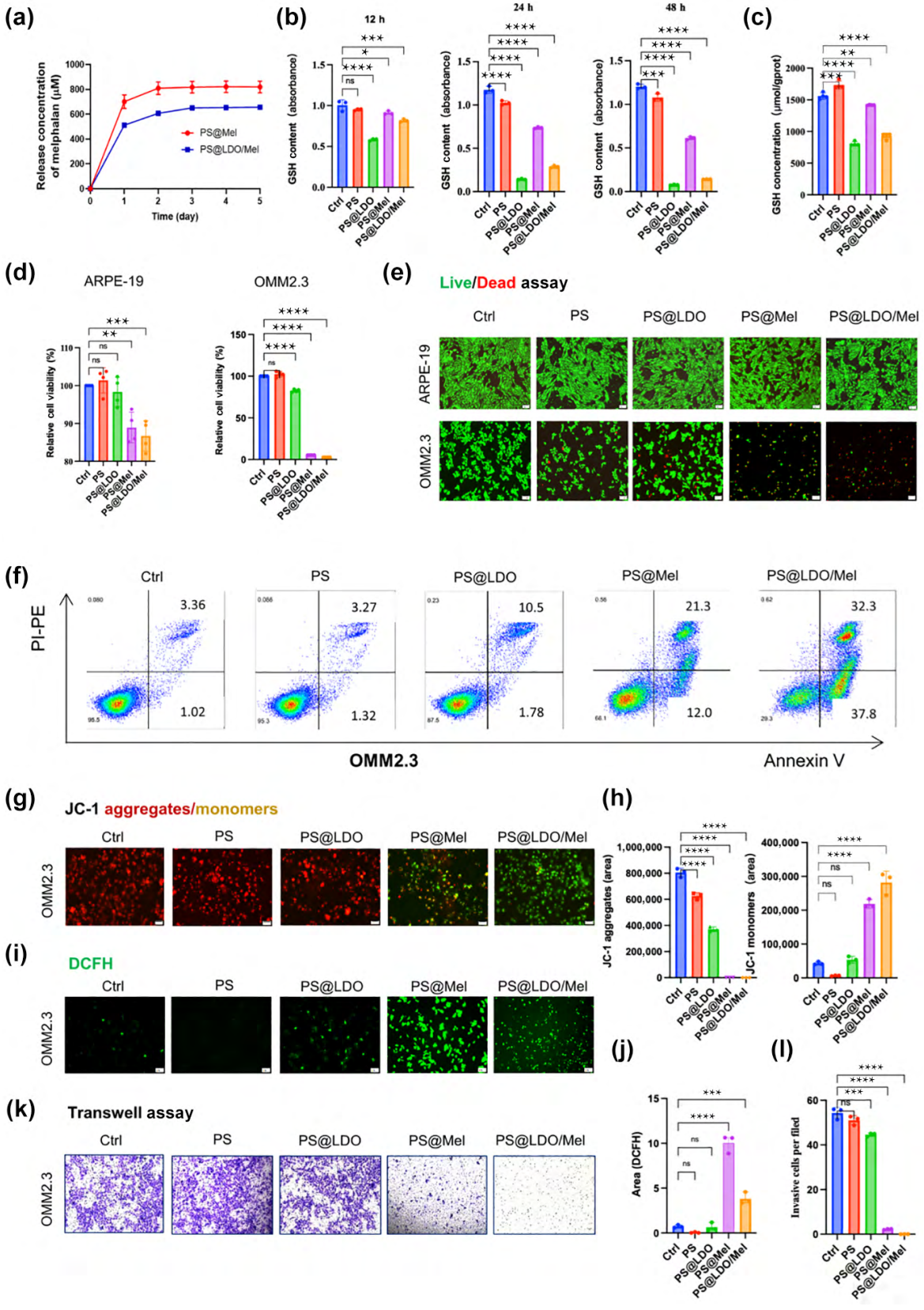

Figure 4 *In vitro* chemosensitization via ROS amplification and GSH depletion. (a) Drug release profile of melphalan. (b) Residual GSH content after hydrogel treatment. (c) Intracellular GSH levels in OMM2.3 cells after co-culture with the hydrogel. Toxicity evaluation of the hydrogel on cells: (d) cell viability assay; and (e) live/dead staining images. Toxicity evaluation of the hydrogel on OMM2.3 cells: (f) apoptosis analysis of hydrogel-treated OMM2.3 cells by flow cytometry, (g) schematic of JC-1 staining, and (h) quantitative analysis of fluorescence results. (i) Schematic of ROS detection by DCFH fluorescence staining and (j) quantitative analysis of fluorescent area. (k) Schematic of OMM2.3 cell invasion by crystal violet staining and (l) quantitative analysis of invasion area.

treatment groups: PBS, PS, PS@LDO, PS@Mel and PS@LDO/Mel. On day 20 post-treatment, tumors were excised for metabolomic analysis (Fig. 5(a)). Histological evaluation of tumor microenvironments revealed that PS@LDO/Mel significantly enhanced chemotherapy efficacy against UM. Hematoxylin and eosin (H&E) staining demonstrated: Control group: extensive tumor infiltration throughout the eyeball, disrupting intraocular structures; PS group: massive tumor proliferation; PS@LDO group: partial confinement of posterior segment tumor growth; PS@Mel group: marked restriction of posterior segment tumor growth; PS@LDO/Mel group: minimal residual tumors (Figs. 5(b) and 5(c)). H&E staining of major organs (heart, liver, kidneys, lungs, and spleen) confirmed no significant histopathological alterations in the PS@LDO/Mel group compared to controls (Fig. 5(d)), validating the systemic safety of the combined therapy.

4 Conclusions

In this study, we developed and optimized a chemotherapy-sensitizing biomaterial, PS@LDO/Mel hydrogel, capable of promoting ROS generation and depleting intracellular GSH. PS@LDO/Mel enabled controlled drug release and significantly enhanced the cytotoxic efficacy of melphalan against uveal melanoma cells. Moreover, the safety and therapeutic efficacy of the hydrogel were systematically validated through multidimensional evaluations. Overall, this study provides mechanistic insights into chemotherapeutic action in uveal melanoma and presents a promising strategy for controlled drug delivery and chemosensitization, with potential implications for future diagnosis and treatment of uveal melanoma.

Electronic Supplementary Material: Supplementary material (high resolution XPS spectrum, POD-like and OXD-like activity at pH = 7.4, live/dead staining images of ARPE-19 and OMM2.3, and other details of experiments) is available in the online version of this article at https://doi.org/10.26599/NR.2026.94908842.

Data availability

All data needed to support the conclusions in the paper are

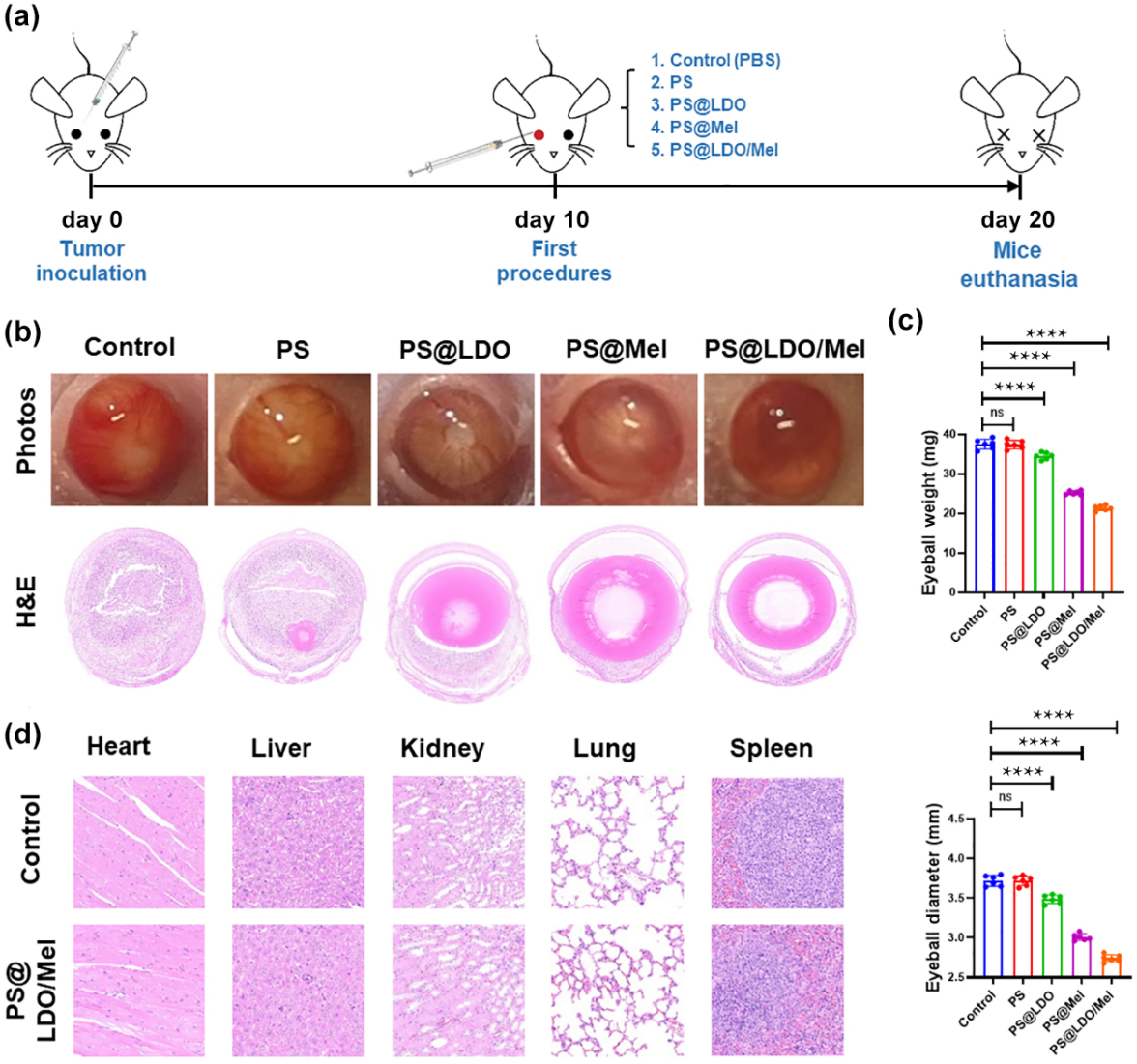

Figure 5 *In vivo* antitumor efficacy and biosafety in uveal melanoma. (a) Schematic of the periocular UM tumor model establishment in mice. (b) Representative photographs and H&E staining of intraocular tumors. (c) Eyeball weight and diameter after various treatments. (d) H&E staining of major organs (heart, liver, kidneys, lungs, and spleen).

presented in the manuscript and/or the Electronic Supplementary Material. Additional data related to this paper may be requested from the corresponding author upon reasonable request.

Acknowledgment

This work was supported by the Key Project of Xuzhou Medical University (No. XYFZ202402).

Declaration of competing interest

The authors declare no conflict of interest.

Author contribution statement

Y. F. Z., A. Z., and S. H. C. designed the experiments. S. Y. Q., L. Y. H., M. Y. L. and Y. X. C. performed the experiments and interpreted the results. X. M. Z. assisted with the data analysis. S. Y. Q. and L. Y. H. wrote the manuscript. A. Z. and S. H. C. reviewed and revised the manuscript.

Informed consent

Not applicable.

Ethics statement

The animal experiments were carried out following the guidelines of the Shanghai Ninth People's Hospital Institutional Committee for the Care and Use of Laboratory Animals and were approved by the Committee on Ethical Use of Animals of Shanghai Ninth People's Hospital (Ethics Code: SH9H-2024-A1369-1).

Use of AI statement

None.

References

[1] Han, D. D.; Li, C. J.; Araimdeh, S.; Sree, V.; Rahimi, E.; Buganza Tepole, A.; Ardekani, A. M. Lymphatic uptake of biotherapeutics through a 3D hybrid discrete-continuum vessel network in the skin tissue. *J. Control. Release* **2023**, *354*, 869–888.

[2] Hu, R. Z.; Chen, X. Y.; Li, Z. F.; Zhao, G. J.; Ding, L.; Chen, L.; Dai, C.; Chen, Y.; Zhang, B. Liquid nanoparticles for nanocatalytic cancer therapy. *Adv. Mater.* **2023**, *35*, 2306469.

[3] Vernekar, A. A.; Das, T.; Ghosh, S.; Mugesh, G. A remarkably efficient $MnFe_2O_4$-based oxidase nanozyme. *Chem. Asian J.* **2016**, *11*, 72–76.

[4] Yan, L.; Gonca, S.; Zhu, G. Y.; Zhang, W. J.; Chen, X. F. Layered double hydroxide nanostructures and nanocomposites for biomedical applications. *J. Mater. Chem. B* **2019**, *7*, 5583–5601.

[5] Chen, S. H.; Xu, R.; Huo, P. P.; Liu, J. Y.; Zhang, D. D.; Qiu, J. J.; Liu, X. Y. Cisplatin and ionic redox pairs co-delivery gelatin/hyaluronic acid hydrogels with amplified chemotherapy/chemodynamic tumor therapy. *Appl. Mater. Today* **2024**, *40*, 102388.

[6] Sarmah, D.; Rather, M. A.; Sarkar, A.; Mandal, M.; Sankaranarayanan, K.; Karak, N. Self-cross-linked starch/chitosan hydrogel as a biocompatible vehicle for controlled release of drug. *Int. J. Biol. Macromol.* **2023**, *237*, 124206.

[7] Gao, W. W.; Zhang, Y.; Zhang, Q. Z.; Zhang, L. F. Nanoparticle-hydrogel: A hybrid biomaterial system for localized drug delivery. *Ann. Biomed. Eng.* **2016**, *44*, 2049–2061.

[8] Jing, G. X.; Yang, L. N.; Wang, H.; Niu, J. T.; Li, Y. Y.; Wang, S. L. Interference of layered double hydroxide nanoparticles with pathways for biomedical applications. *Adv. Drug Deliv. Rev.* **2022**, *188*, 114451.

[9] Zhang, L. X.; Hu, J.; Jia, Y. B.; Liu, R. T.; Cai, T.; Xu, Z. P. Two-dimensional layered double hydroxide nanoadjuvant: Recent progress and future direction. *Nanoscale* **2021**, *13*, 7533–7549.

[10] Rathee, G.; Kohli, S.; Singh, N.; Awasthi, A.; Chandra, R. Calcined layered double hydroxides: Catalysts for xanthene, 1, 4-dihydropyridine, and polyhydroquinoline derivative synthesis. *ACS Omega* **2020**, *5*, 15673–15680.

[11] Wei, H.; Wang, E. Nanomaterials with enzyme-like characteristics (nanozymes): Next-generation artificial enzymes. *Chem. Soc. Rev.* **2013**, *42*, 6060–6093.

[12] Cao, S. J.; Zhao, Z. Y.; Zheng, Y. J.; Wu, Z. H.; Ma, T.; Zhu, B. H.; Yang, C. D.; Xiang, X.; Ma, L.; Han, X. L. et al. A library of ROS-catalytic metalloenzyme mimics with atomic metal centers. *Adv. Mater.* **2022**, *34*, 2200255.

[13] Niu, B. Y.; Liao, K. X.; Zhou, Y. X.; Wen, T.; Quan, G. L.; Pan, X.; Wu, C. B. Application of glutathione depletion in cancer therapy: Enhanced ROS-based therapy, ferroptosis, and chemotherapy. *Biomaterials* **2021**, *277*, 121110.

[14] Chen, Y. L.; Cai, Y. J.; Yu, X. S.; Xiao, H.; He, H. Z.; Xiao, Z. C.; Wang, Y.; Shuai, X. T. A photo and tumor microenvironment activated nano-enzyme with enhanced ROS generation and hypoxia relief for efficient cancer therapy. *J. Mater. Chem. B* **2021**, *9*, 8253–8262.

[15] Wang, Y.; Yang, M. R.; Zhao, Z. Facile fabrication of self-healing, injectable and antimicrobial cationic guar gum hydrogel dressings driven by hydrogen bonds. *Carbohydr. Polym.* **2023**, *310*, 120723.

[16] Kang, T.; Cha, G. D.; Park, O. K.; Cho, H. R.; Kim, M.; Lee, J.; Kim, D.; Lee, B.; Chu, J.; Koo, S. et al. Penetrative and sustained drug delivery using injectable hydrogel nanocomposites for postsurgical brain tumor treatment. *ACS Nano* **2023**, *17*, 5435–5447.

[17] Shi, K. J.; Fu, W. J.; Farhadi Sabet, Z.; Ye, J. M.; Liang, S. J.; Liu, T.; Liu, Q. L.; Guo, M. Y.; You, M.; Wu, J. G. et al. Hydrogel-mediated jamming of exosome communications that counter tumor adaption in the tumor immune microenvironment. *ACS Nano* **2024**, *18*, 33042–33057.

[18] Cai, Y.; Xin, L. Y.; Li, H.; Sun, P.; Liu, C.; Fang, L. Mussel-inspired controllable drug release hydrogel for transdermal drug delivery: Hydrogen bond and ion-dipole interactions. *J. Control. Release* **2024**, *365*, 161–175.

[19] Zhao, W. J.; Su, R.; Huang, Y. Q.; Wu, J. Q.; Fong, C. F.; Feng, J. G.; Xiong, Q. H. Transient circular dichroism and exciton spin dynamics in all-inorganic halide perovskites. *Nat. Commun.* **2020**, *11*, 5665.